THREE-DIMENSIONAL PHISICAL MODELING OF LANDSLIDE-GENERATED TSUNAMIS

Tomoyuki Takabatake, Kindai University, takabatake@civileng.kindai.ac.jp
Dawn Chenxi Han, Waseda University, dawnhan@akane.waseda.jp
Miguel Esteban, Waseda University, esteban.fagan@gmail.com
Tomoya Shibayama, Waseda University, shibayama@waseda.jp

INTRODUCTION

Massive landslides can generate significant tsunamis and endanger coastal communities, as shown by recent catastrophic events such as the 2018 Palu Tsunami and 2018 Sunda Strait Tsunami (e.g., Heidarzadeh et al. 2018; Takabatake et al. 2019). While a number of experimental studies have been conducted to investigate landslide-generated tsunamis, most were performed using two-dimensional (2D) wave flumes (e.g., Fritz et al. 2004; Takabatake et al. 2020). Thus, the present study conducted three-dimensional (3D) experiments to clarify the characteristics of landslide-generated tsunamis, and to develop empirical equations that can predict the generated wave heights and periods.

METHODOLOGY

Experiments were conducted using a 3D wave basin at Waseda University, Japan (Figure 1) with the same setup of Takabatake et al. (2022). A total of 114 different experimental cases (consisting of 23 subaerial and 91 partially-submerged landslides ones) were performed by varying the landslide mass (m), slope angle (α), initial water depth (h), gate height (h_i), initial submergence depth (h_s), and vertical-drop distance (h_a) (see Takabatake et al. [2022] for further information about these parameters). In the experiments, landslides (modeled using glass beads) were generated by instantaneously opening a lift gate. Time series of water surface elevations were recorded using twelve wave gauges (WGs), located at r = 1.0 m (WG1-WG5), 2.0 m (WG6-WG10), and 3.75 m (WG11-WG12) (see Figure 1).

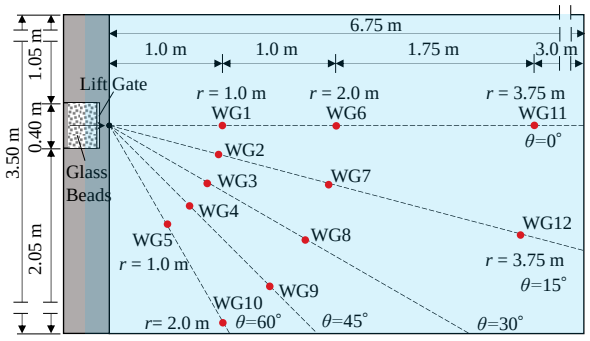

Figure 1 - Experimental setup (not to scale).

RESULTS

Obtained results are summarized in Figures 2 and 3 for the subaerial and partially-submerged landslide cases, respectively. As shown in Figures 2a and 3a, the leading crest wave amplitudes (a_{c1_a} for subaerial, and a_{c1_p} for partially-submerged cases) in the near-field zone (r = 1.0 m, namely at WG1-WG5 in Figure 1) were found to decrease according to the increase in the propagation angle (θ) for both landslide types. For instance, the leading crest wave amplitudes recorded at WG1 (θ = 0°) were on average 1.7 times greater than those at WG5 (θ = 60°) for the partially-submerged landslides. Figures 2b and 3b show the mean leading crest wave amplitudes averaged over all experimental cases (for each type of landslide) at each WG. As shown, mean leading crest wave amplitudes decayed with the propagation distance (r), and higher rates of decay were observed with the smaller propagation angles. Figures 2c and 3c show the wave period of the leading wave (T_{c1_a} for subaerial, and T_{c1_p} for partially-submerged cases) recorded at r = 1.0 m. In contrast to the wave amplitudes, there were no clear differences in the wave periods according to the propagation angles, with the range of $T_{c1}(g/h)^{0.5}$ being mostly distributed from 5 to 10 (regardless of the propagation angles and landslide types). The wave periods averaged over all the cases (for each type of landslide) at each WG are shown in Figures 2d and 3d. They demonstrated that the wave periods increased according to the propagation distance. For instance, the leading wave periods recorded at r = 3.75 m were on average 1.3 times greater than those at r = 1.0 m for the partially-submerged landslides. When comparing the generated waves with the applicability ranges of different wave theories (the leading waves were assumed to be periodic and permanent), they were located in the intermediate water depth regime, indicating that wave dispersion effects were not negligible. Thus, the reduction in the wave amplitude and increase in the wave period according to the propagation distance could be attributed to wave dispersion effects.

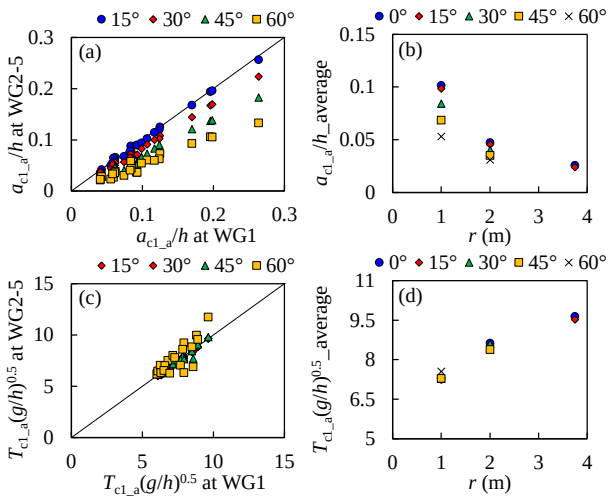

Figure 2 - Comparison of the (a) leading crest wave amplitudes at r = 1.0 m, (b) mean wave amplitudes for each WG, (c) wave periods at r = 1.0 m, and (d) mean wave periods for each WG for subaerial landslides.

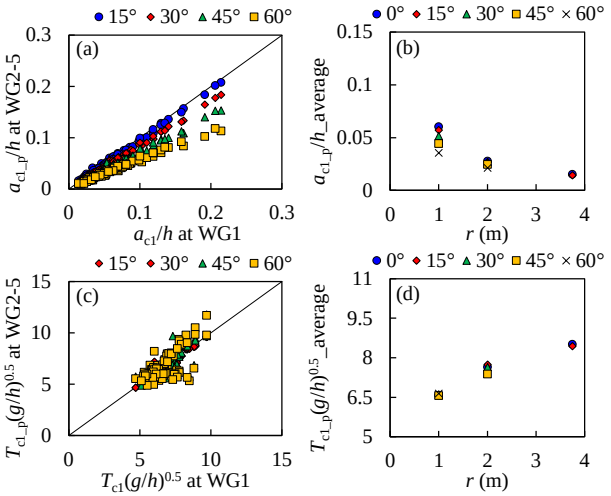

Figure 3 - Comparison of the (a) leading crest wave amplitudes at r = 1.0 m, (b) mean wave amplitudes for each WG, (c) wave periods at r = 1.0 m, and (d) mean wave periods for each WG for partially-submerged landslides.

A multiple regression analysis was also applied to the obtained dataset, and predictive equations to estimate the crest wave amplitudes and wave periods were developed for each of the subaerial and partially-submerged landslides as shown in Equations (1)-(4).

$$\frac{a_{c1\_a}}{h} = 0.37\left(\frac{m}{\rho_w b h^2}\right)^{1.66}\left(\frac{h_a}{h}\right)^{-1.08}\left(\frac{h_i}{h}\right)^{1.37} \times (\cos\theta)^{0.74}(\tan\alpha)^{0.52}\left(\frac{r}{h}\right)^{-0.98} \quad (1)$$

$$\frac{a_{c1\_p}}{h} = 0.14\left(\frac{m}{\rho_w b h^2}\right)^{1.24}\left(\frac{h_s}{h}\right)^{-0.33}\left(\frac{h_i}{h}\right)^{0.44} \times (\cos\theta)^{0.45}(\tan\alpha)^{0.22}\left(\frac{r}{h}\right)^{-0.94} \quad (2)$$

$$T_{c1\_a}\left(\frac{g}{h}\right)^{0.5} = 5.28\left(\frac{m}{\rho_w b h^2}\right)^{0.25}\left(\frac{h_a}{h}\right)^{-0.26}\left(\frac{h_i}{h}\right)^{0.27} \times (\cos\theta)^{0.06}(\tan\alpha)^{0.12}\left(\frac{r}{h}\right)^{0.20} \quad (3)$$

$$T_{c1\_p}\left(\frac{g}{h}\right)^{0.5} = 4.49\left(\frac{m}{\rho_w b h^2}\right)^{0.09}\left(\frac{h_s}{h}\right)^{-0.08}\left(\frac{h_i}{h}\right)^{-0.06} \times (\cos\theta)^{0.09}(\tan\alpha)^{0.07}\left(\frac{r}{h}\right)^{0.18} \quad (4)$$

where ρ_w is the density of water. Notably, while the wave decay term (r/h) has a negative exponent for crest wave amplitudes, it has a positive exponent for wave periods, which is in line with the tendency observed in the previous findings. Figures 4a and 4b show the comparison of a_{c1_a} and a_{c1_p} measured in the experiments of the present study and those predicted by the developed equations. As shown, most of the plots were located within the error bounds of ±30%. The calculated correlation coefficients were 0.94 (for subaerial landslides) and 0.91 (for partially-submerged landslides), respectively, indicating that the developed equations could predict the wave amplitudes with relatively good accuracy. Figures 4c and 4d compare the measured wave periods with the predicted ones. While they were also relatively well predicted by the developed equations, the calculated correlation coefficients were lower than those for crest wave amplitudes with 0.81 (for subaerial landslides) and 0.67 (for partially-submerged landslides), respectively.

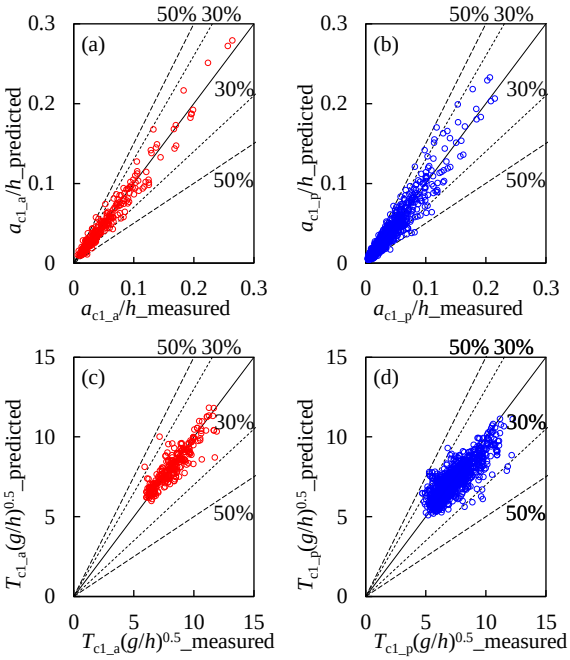

Figure 4 - Comparison of the crest amplitudes of the leading waves measured and predicted ones for (a) subaerial and (b) partially-submerged landslides, and that of the wave periods for (c) subaerial and (d) partially-submerged landslides.

CONCLUSIONS

The characteristics of landslide-generated tsunamis were investigated by performing a total of 114 experiments at a 3D wave basin. Based on the obtained dataset, empirical equations were also developed to predict wave amplitudes and periods, which would aid in the rapid assessment of a tsunami hazard.

REFERENCES

Fritz et al. (2004): Near Field Characteristics of Landslide Generated Impulse Waves. *J. Waterw. Port Coast. Ocean Eng.*, vol. 130(6), pp. 287-302.

Heidarzadeh et al. (2018): Insights on the Source of the 28 September 2018 Sulawesi Tsunami, Indonesia Based on Spectral Analyses and Numerical Simulations. *Pure Appl. Geophys.*, vol. 176, pp. 25-43.

Takabatake et al. (2019): Field Survey and Evacuation Behaviour during the 2018 Sunda Strait Tsunami. *Coast. Eng. J.*, vol.61(4), pp. 423-443.

Takabatake et al. (2020): Physical Modeling of Tsunamis Generated by Subaerial, Partially Submerged, and Submarine Landslides. *Coast. Eng. J.*, vol. 62(4), pp. 582-601.

Takabatake et al. (2022): Three-Dimensional Physical Modelling of Tsunamis Generated by Partially Submerged Landslides. *J. Geophys. Res. Oceans*, e2021JC017826.